

pubs.acs.org/acssensors Article

Multiscale Assay of Unlabeled Neurite Dynamics Using Phase Imaging with Computational Specificity

Mikhail E. Kandel,[#] Eunjae Kim,[#] Young Jae Lee, Gregory Tracy, Hee Jung Chung, and Gabriel Popescu*



Cite This: ACS Sens. 2021, 6, 1864-1874



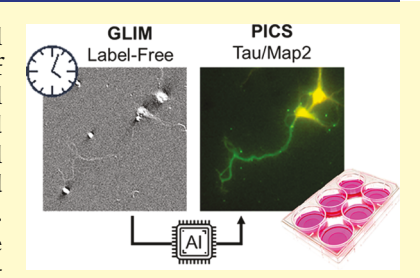
ACCESS

III Metrics & More

Article Recommendations

Supporting Information

ABSTRACT: Primary neuronal cultures have been widely used to study neuronal morphology, neurophysiology, neurodegenerative processes, and molecular mechanism of synaptic plasticity underlying learning and memory. However, the unique behavioral properties of neurons make them challenging to study, with phenotypic differences expressed as subtle changes in neuronal arborization rather than easy-to-assay features such as cell count. The need to analyze morphology, growth, and intracellular transport has motivated the development of increasingly sophisticated microscopes and image analysis techniques. Due to its high-contrast, high-specificity output, many assays rely on confocal fluorescence microscopy, genetic methods, or antibody staining techniques. These approaches often limit the ability to measure quantitatively dynamic activity such as intracellular transport and



growth. In this work, we describe a method for label-free live-cell cell imaging with antibody staining specificity by estimating the associated fluorescence signals via quantitative phase imaging and deep convolutional neural networks. This computationally inferred fluorescence image is then used to generate a semantic segmentation map, annotating subcellular compartments of live unlabeled neural cultures. These synthetic fluorescence maps were further applied to study the time-lapse development of hippocampal neurons, highlighting the relationships between the cellular dry mass production and the dynamic transport activity within the nucleus and neurites. Our implementation provides a high-throughput strategy to analyze neural network arborization dynamically, with high specificity and without the typical phototoxicity and photobleaching limitations associated with fluorescent markers.

KEYWORDS: microscopy, quantitative phase imaging, neuronal cell culture, artificial intelligence, fluorescence microscopy, high-content screening, PICS, label-free imaging

euronal branching and arborization provide a phenotypic marker for cellular viability and neurogenerative diseases.¹⁻⁴ While phase contrast microscopy can be used for studying neuronal cultures,⁵ the resulting images often struggle to differentiate between neurons and glia⁶ and offer little beyond qualitative morphological information. Due to the need for chemical specificity, fluorescence-based techniques have become the main tools in neuroscience. For example, confocal microscopy used in combination with immunostaining can reliably study axonal growth and dendritic branching.8 When cells are fixed, dynamic information is painstakingly extracted by recording images from different subpopulations at different times. These challenges motivated the use of fluorescence proteins, which in turn introduces restrictions, such as phototoxicity and throughput, the transfection process often hampering experiments with limited timeframes.¹²

Quantitative phase imaging (QPI),^{13–15} which derives morphology information from the scattered light by unlabeled specimens, offers a nondestructive method for studying cellular dynamics. This is accomplished by using interferometry to extract intrinsic information about the scattering potential associated with the object. As the scattering potential is

invariant to the imaging system, it can be used to measure physical parameters such as the dry mass content of the cell. 16-19 In a broader context, QPI techniques promise to improve the image sensitivity to nostructures, 20 facilitate 3D imaging, 21-23 and reduce observational bias due to staining 24 and fluorescent labels. 25-29 Although the quantitative phase measurement adds new information to the transmitted light signal, it nevertheless lacks molecular specificity. However, recent progress in artificial intelligence offers a potential solution. With the advent of artificial intelligence techniques based on deep convolutional neural networks, 30 a new image-to-image translation 31,32 strategy has emerged where artificial stains can be inferred from the quantitative phase image itself. 33 Exploiting the high sensitivity to structure and quantitative information, phase imaging with computational

Received: January 16, 2021 Accepted: April 9, 2021 Published: April 21, 2021





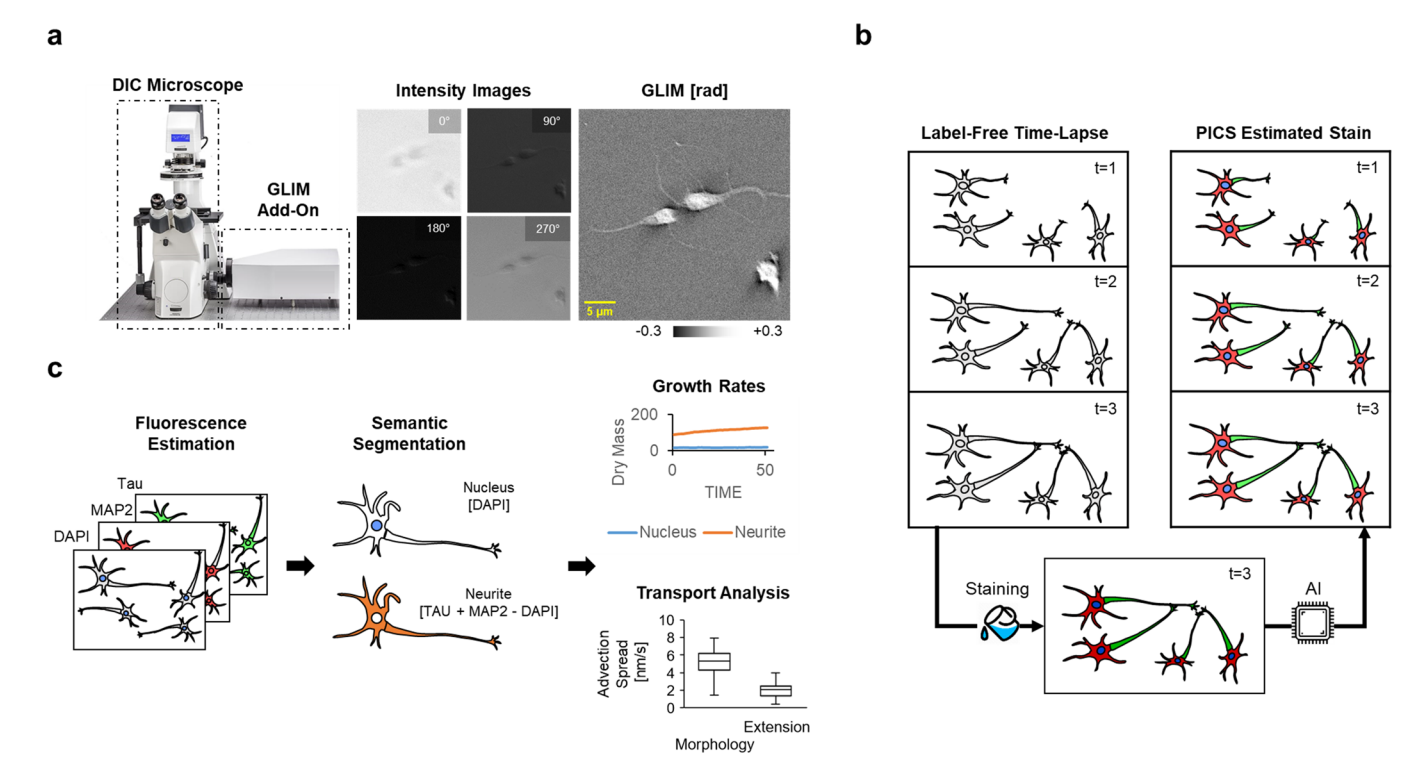


Figure 1. Phase imaging with computational specificity (PICS) for measuring growth and transport during neural arborization. (a) The GLIM system upgrades a conventional differential interference contrast microscope with quantitative phase imaging capabilities. (b) Hippocampal cultures were imaged over 41 h for time-lapse analysis (20×/0.8). After the recording, neurons were fixed and stained with antibodies for Tau and MAP2 to obtain colocalized phase and fluorescence images. An additional nucleus (DAPI-like) channel is provided by manual annotation. To recover time-lapse data with specificity to antibodies, deep convolutional neural networks trained on the fixed cells were used to infer the fluorescence signals on live cells. (c) PICS (inferred fluorescence) maps for Tau, MAP2, and nuclei created a three-channel semantic segmentation map, labeling the image as "background", "nucleus", and "neurite". The segmentation map is then used to characterize the neural growth rates and intracellular mass transport.

specificity (PICS) was used to characterize the dry mass growth rate of subcellular compartments.³⁴

The intersection of quantitative phase imaging and artificial intelligence is not without precedent. The newfound ability for AI to annotate images has been used for diverse applications such as identifying cellular nuclei²⁸ and predicting fertility outcomes associated with sperm cell morphology.³⁵ In a more unconventional direction, AI has been shown to provide an avenue for estimating data that fall outside the imaging instrument's traditional sensitivity, such as imputing data inside the missing cone³⁶ or even estimating polarization states.³⁷ These efforts show that AI techniques facilitate disambiguating physical phenomena that are challenging to describe under classical, non-data-driven formulations. In more modest terms, AI has been used to improve API imaging instrumentation, for example, by providing an autofocusing system³⁸ or removing "coherent" artifacts associated with fringe-based interferometers.^{39,40}

In this work, we show that PICS can be used to measure the arborization process in unlabeled neural cultures, over multiple days, nondestructively (Figure 1). Our method consists of highly sensitive QPI as well as end-to-end image analysis to infer the fluorescence intensity for Tau and MAP2, ⁴¹ commonly used to identify axons and dendrites. These PICS-derived fluorescence images are then used to label the neuronal compartments with subcellular specificity. To capture subcellular growth and intracellular transport, we apply the PICS-derived semantic segmentation maps to the dry mass density images rendered by QPI. We validated our assay by

performing a high-content screening of early-stage hippocampal cultures and observed several remarkable relationships between dry mass transport and growth in neurons.

RESULTS

PICS Workflow for Semantic Segmentation. PICS combines highly sensitive, temporally stable QPI with deep learning to estimate fluorescence stains from unlabeled specimens. (Figure 1). The inferred fluorescence signal is processed to generate semantic segmentation maps, which are then used to analyze the transport and growth of the cellular dry mass. To acquire the quantitative phase images, we use gradient light interference microscopy (GLIM), which measures the optical path length shifts associated with the specimen in a differential interference contrast (DIC) geometry. In short, GLIM was used in this study to measure quantitative parameters, improving the image quality in DIC while maintaining the fluorescence signal.⁴² Furthermore, the GLIM module⁴³ is a relatively straightforward modification to the conventional DIC microscope (Supplementary Note 1).

Following the procedure in Figure 2 (see Supplementary Note 1 for details), we acquire four intensity frames corresponding to $\pi/2$ offsets between the two laterally shifted beams in DIC. The interference between these two beams reveals the derivative of the phase map along the direction of the shift. The QPI map is obtained by integrating this derivative using a Hilbert transform (Supplementary Figure 1c). To identify axons and dendrites, we performed antibody staining for the Tau and MAP2 proteins, respectively. As the

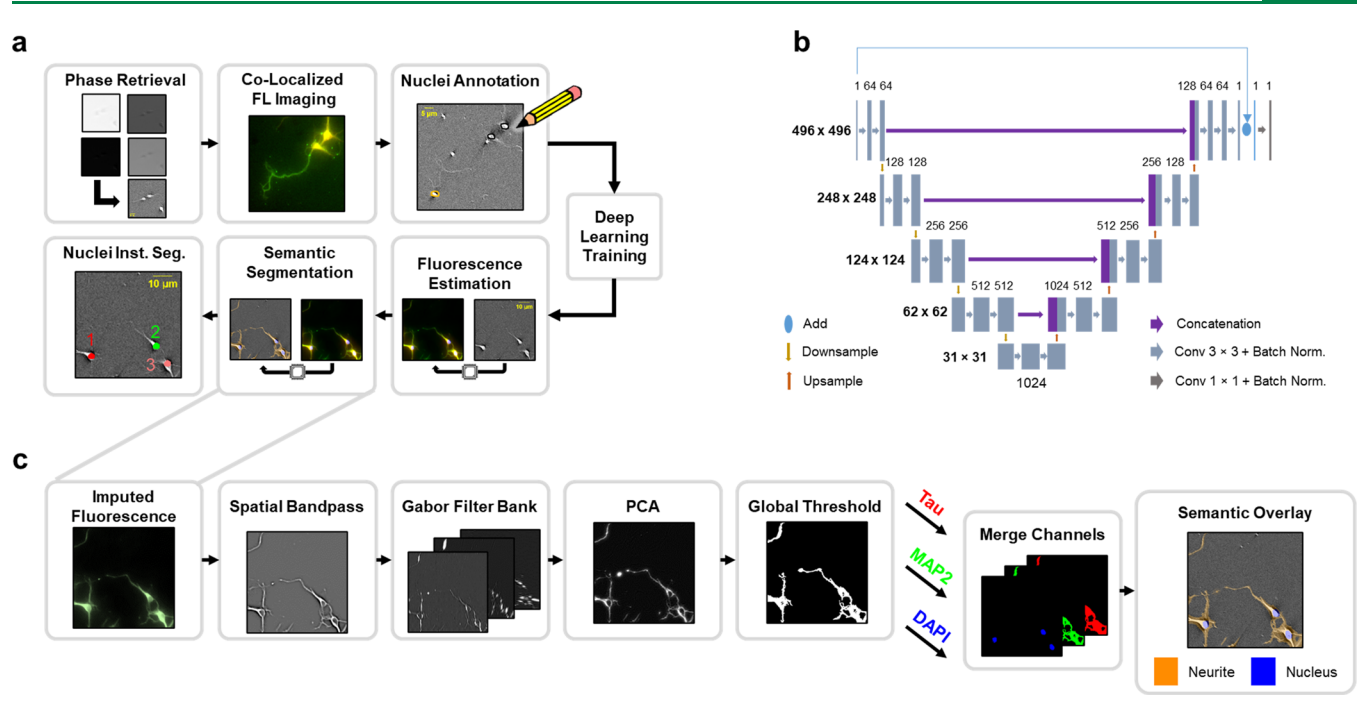


Figure 2. Workflow for automatically annotating GLIM images. (a) Colocalized GLIM and FL images were digitally registered. The phase data were reconstructed using a Hilbert transform integration technique. Nuclei were manually annotated in ImageJ to simulate DAPI staining. A deep convolutional neural network was trained using measured data to reproduce the fluorescence channels (Tau/MAP2/DAPI) from the label-free GLIM image. To analyze dry mass growth rates, we performed inference on the unstained time-lapse sequence. The estimated fluorescence is converted into a semantic segmentation map with labels for neurite, nucleus, and background. Finally, connected component analysis on the nucleus-associated regions is used to produce instance segmentation to count the number of nuclei in each field of view. (b) Images are trained using a U-Net architecture consisting of 64 filters at the first layer, and a Pearson correlation between the actual and estimated fluorescence is used as the loss function. (c) Estimated fluorescence maps are processed to obtain a binary map by applying a spatial bandpass, generating textures using a Gabor filter bank, and reducing the dimensionality with principal component analysis. Finally, a threshold is applied to binarize the image for each channel. These three channels are then merged to form an annotated image with labels for the neurite, nucleus, and background.

detection light paths in transmission and epi-fluorescence are shared, it is straightforward to acquire colocalized fluorescence images using the same camera detector. Furthermore, we included a PICS DAPI label by manually annotating the nuclei in the phase images. Here, we preferred manual annotation to avoid an extra fluorescence channel and potentially photobleach the sensitive antibody stains.

These colocalized fluorescence images are used to train neural networks that estimate the fluorescence image from the transmitted light GLIM image. We note that, while the four frames that constitute the GLIM image took approximately 200 ms to acquire, each fluorescence channel was acquired by averaging a total of 10 images at 700 ms exposure each, with 2 × 2 binning. Thus, we found that fluorescence microscopy was 70× slower than phase imaging. While antibody staining is often faint and depends on protein expression, the signal in transmitted light imaging can be modulated by simply increasing the strength of the illumination (with no risk of photobleaching). These results highlight an important throughput advantage of synthetic rather than physical staining.

Next, we use the neural networks trained on fixed, antibodystained cells to perform inference on the unstained live neurons. As shown in Figure 2c, the estimated fluorescence signal is converted into a semantic segmentation map through a series of image processing steps. For each estimated fluorescence image, we perform a spatial bandpass²⁰ to remove low frequencies and generate a series of variants of the image using a Gabor filter bank.⁴⁵ The resulting set of images highlights the textural information and contains many values at each pixel. The parameters are reduced to a single channel by principal component analysis (PCA),⁴⁶ with a global threshold applied to binarize the image. Compared to simpler global thresholding approaches that rely on histogram analysis, Gabor filters capture textural information, which allows for a more accurate segmentation.

This procedure is repeated to generate a binary map for each channel (Tau and MAP2). To merge the channels into a three-category semantic segmentation map ("nucleus", "neurite", and "background"), we take the nuclear binary map, add the Tau and MAP2 binary images, and assign the "background" label to the rest of the pixels. We merged the Tau and MAP2 channels to increase the signal-to-noise ratio and study the growth and dynamics of both axons and dendrites. As shown in Supplementary Note 3 and Supplementary Table 1, we find good agreement between the semantic maps generated from the estimated and actual fluorescence signals.

Finally, we perform instance segmentation to count the nuclei by simple connected component analysis (CCA)⁴⁷ on the binary nucleus-associated labels. We validated our cell counting technique by comparing manual to automatic nuclear counts at the first time point. We obtained a Pearson correlation coefficient of 0.94 between the two techniques, with the principal disagreement stemming from cell clusters and glia cells. The manual cell count took roughly 3 h to perform, while the CCA-based method was completed in under a minute.

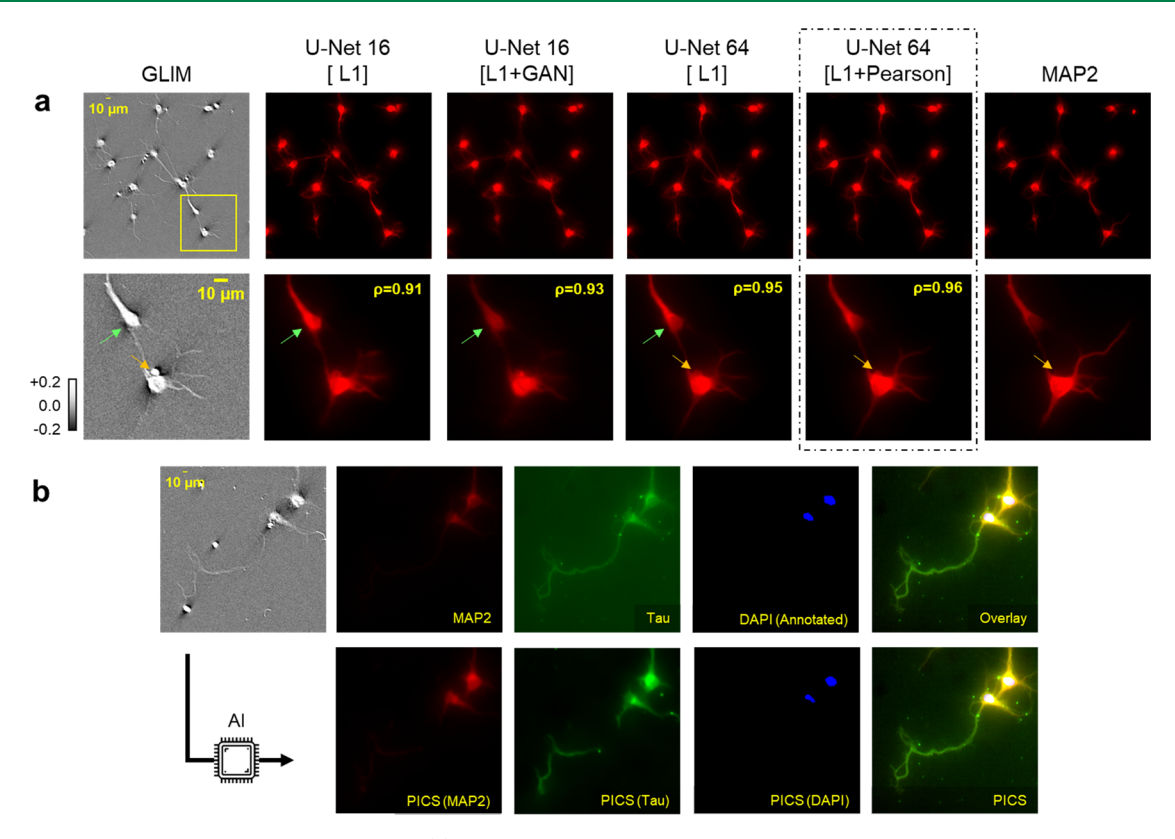


Figure 3. Deep convolutional neural network training. (a) To investigate the effect of neural network architecture loss functions on image quality, we measured the Pearson correlation between the actual and estimated fluorescence images. As a baseline for performance, we took a U-Net constructed with a reduced parameter set consisting of 16 initial filter elements trained against an L1 loss function. Compared with the conventional U-Net training scheme, we found that a GAN improved performance by suppressing the overestimation of MAP2 concentration in the nucleus (green arrows). Further improvements came from expanding the number of filters in the U-Net architecture, with the GAN removed for faster training time (U-Net 64). Switching the loss function to the Pearson correlation further improved performance with the resulting images suppressing artifacts, such as unwanted debris around the nuclei (U-Net 64, Pearson, orange arrow). (b) Actual vs estimated fluorescence images showed strong agreement, with only a slight mismatch in long axons (20×/0.8).

Neural Network Architecture. Central to our approach is the estimation of fluorescence images from the unlabeled phase maps. To accomplish this, we performed image-to-image translation using a deep convolutional neural network. Deep convolutional neural networks are well suited to this task as they combine the texture-based techniques with added nonlinearities hidden in their deep layers. We used the U-Net architecture, which includes downsampling and upsampling paths to efficiently integrate both textural and contextual information.

To arrive at the final architecture used to estimate our fluorescent tags, we tuned the number of filter banks and trained the network with an unconventional loss function. The results of these experiments are summarized in Figure 3. We selected the architecture in ref 34 as it is known to have a near real-time inference performance on commodity computing hardware, with a filter bank of 16 filter elements at the input layer (Figure 3, "U-Net 16"). All networks were trained against an L1 reconstruction loss function. 49 While able to reproduce much of the morphology of the MAP2 signal ($\rho = 0.91$), the network was poor at capturing variations of protein within cells, often being unable to reject the MAP2 signal within the nucleus (Figure 3, green arrows). To bias the training procedure but maintain the same inference time, we introduced a generative adversarial network (GAN)⁵⁰ training scheme where the U-Net is taken as a generator, and PatchGan was used as a discriminator. 31 Although performance improved

as evidenced by a reduction in the overstaining of the top neuron and an improved correlation coefficient (Figure 3, green arrow, $\rho = 0.93$), the nucleus within the top neuron appeared to be distorted. Attributing these defects to the tendency of GANs to introduce features where none exist,5 we instead removed the GAN and expanded the initial filter bank size to 64 elements (U-Net 64). With more filters, this scheme is more successful in capturing subtle details, and the nuclear vs non-nuclear area is clearly delimited in the top neuron (Figure 3, green arrow). Finally, we modified the loss function to use the Pearson correlation between the actual and estimated fluorescence image, which is our ultimate quality metric.⁵² The resulting network was able to delineate cellular morphology and discriminate between cell bodies and cellshaped debris (Figure 3, orange arrow). Qualitatively, the estimated fluorescence signal shows a strong resemblance to the actual fluorescence signal (Figure 3b). Unlike the real stain, the estimated fluorescence signal avoids autofluorescence and other unwanted sources of noise, especially in the background (Figure 3b, Tau).

Time-Lapse Antibody Staining Prediction. Among the chief advantages of the proposed method is the ability to perform live-cell imaging with the specificity of computationally inferred stains that would otherwise require fixation. This is especially true of antibody-based staining techniques, which require the cell to be cross-linked and made permeable, a procedure that is incompatible with live-cell imaging.⁴¹ To

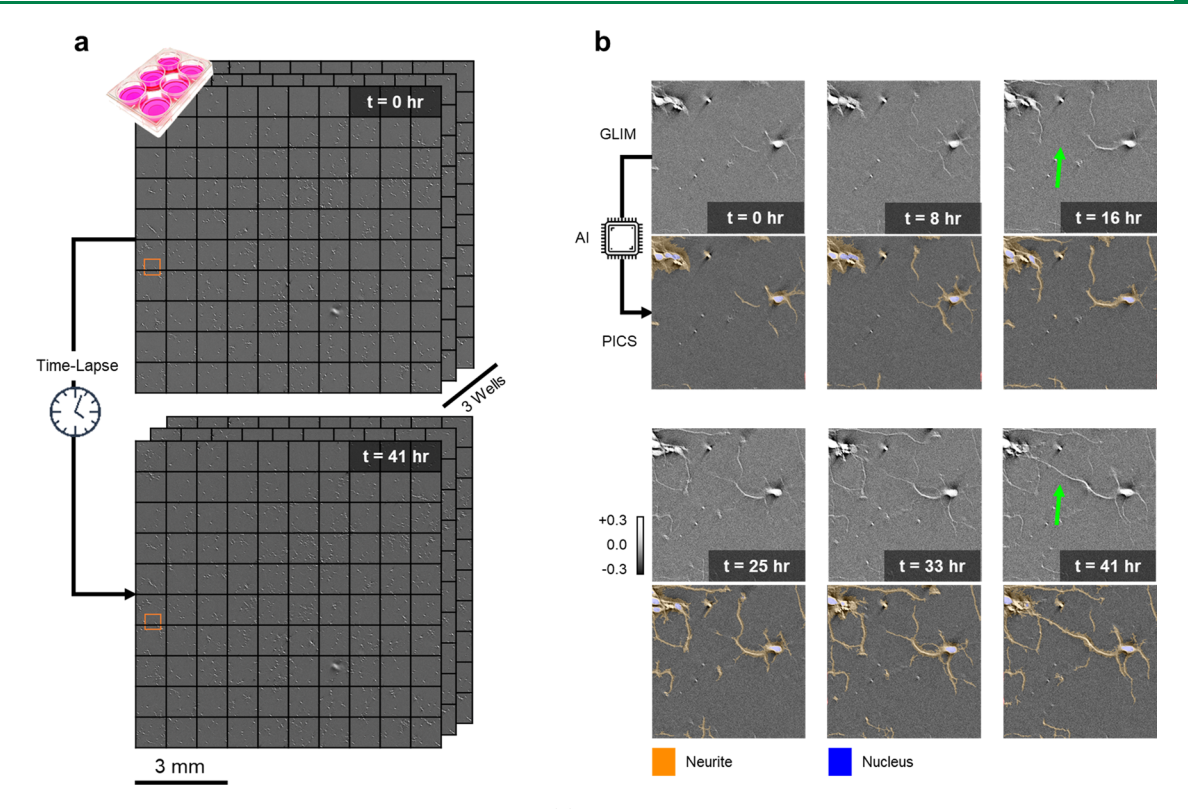


Figure 4. PICS provides antibody specificity to unlabeled live cells. (a) Forty-one hours of time-lapse mosaic imaging was performed on a six-well plate, with three mosaics scans (10×10 images, 5×5 mm²) acquired at each time point. The plate was digitized in under 2 min. (b) Zoomed-in portion of a representative region (orange box) shows increasing arborization as the neurons connect ($20 \times /0.8$).

overcome this challenge, we performed time-lapse GLIM imaging over a few days and stained the cells at the end of the experiment for neural network training. The characterization of primary hippocampal neuronal arborization has been recognized as valuable for applications including drug discovery and toxicity screening^{53,54} (Figure 4).

We imaged early-stage hippocampal neurons consisting of three 5 × 5 mm² regions under a 20×/0.8 objective in a multiwell plate that is typically used to image several preparations in parallel (Figure 4). Each well was imaged by GLIM in roughly half a minute (see Supplementary Figure 2 for details). As per our protocol outlined in Figure 1b, at the end of the experiment, the cells were fixed, immunostained, and imaged by both GLIM and fluorescence microscopy. Next, we trained the neural networks to perform a remapping from the GLIM image to the colocalized fluorescence images, which are then processed into a semantic segmentation map (Figure 2 and Supplementary Figure 3). Importantly, with an efficient GLIM light budget, we can trade exposure time for reduced light intensity and reduced toxicity, which is especially important for imaging highly sensitive cells such as neurons. ⁵⁵

We observed that dendrites show steadier growth when compared to axons, which appear to actively search for connections. We also witnessed that, when a cluster is approached by an axon, it will rapidly divert its dendrite to form a connection 56 (Figure 4, hour 33 to 41, green arrow). These behaviors, as well as others, are shown in Supplementary Movies 1-3.

Mass Transport Analysis. Cells often express dynamic phenotypes that are related to changes in the transport of cellular cargo. To analyze the transport of the cellular mass, we employed dispersion-relation phase spectroscopy (DPS),

which reports on the transport rate of the dry mass at different spatial scales.⁵⁷ Our analysis method is discussed in Supplementary Note 4 with a pictorial representation of the processing steps shown in Supplementary Figure 4.

In DPS, cellular material is understood to be governed by the diffusion—advection equation so that it is possible to measure the spread in advection velocities associated with active cellular transport. DPS has been previously applied to measuring transport in live cells.^{24,58} However, here we used DPS in combination with PICS segmentation, which allows for studying dynamic transport in subcellular compartments. Using the high-throughput AI-based segmentation, we measured the transport associated with 300 fields of view or 4679 neurons.

As shown in Figure 5, we measured cellular dynamics at three spatial scales, with small scales ($\lambda_S = [1.1,2.1] \mu m$) corresponding to the size of dendritic spines and nucleoli, medium scales ($\lambda_{\rm M}$ = [2.1,4.2] μ m) approximately at the width of the extensions, and large scales ($\lambda_L = [4.2500]$) on the order of the cell size. Following the DPS procedure outlined in Supplementary Figure 4, we estimated the variance of the temporal power spectrum at each Fourier frequency in the image sequence. This procedure estimates the activity at each spatial mode (Fourier frequency), with a linear curve fit taken at three relevant spatial frequencies (Supplementary Figure 4). We performed this analysis for the mass that falls within the neurite and nucleus by setting to zero the dry mass values that lie outside the categories. In this work, we looked at transport at relatively long temporal scales, meaning that fast-moving diffusive particles are unlikely to be captured between imaging intervals. Thus, we found that most fields of view were dominated by advection, i.e., temporal bandwidth, Γ , linear in

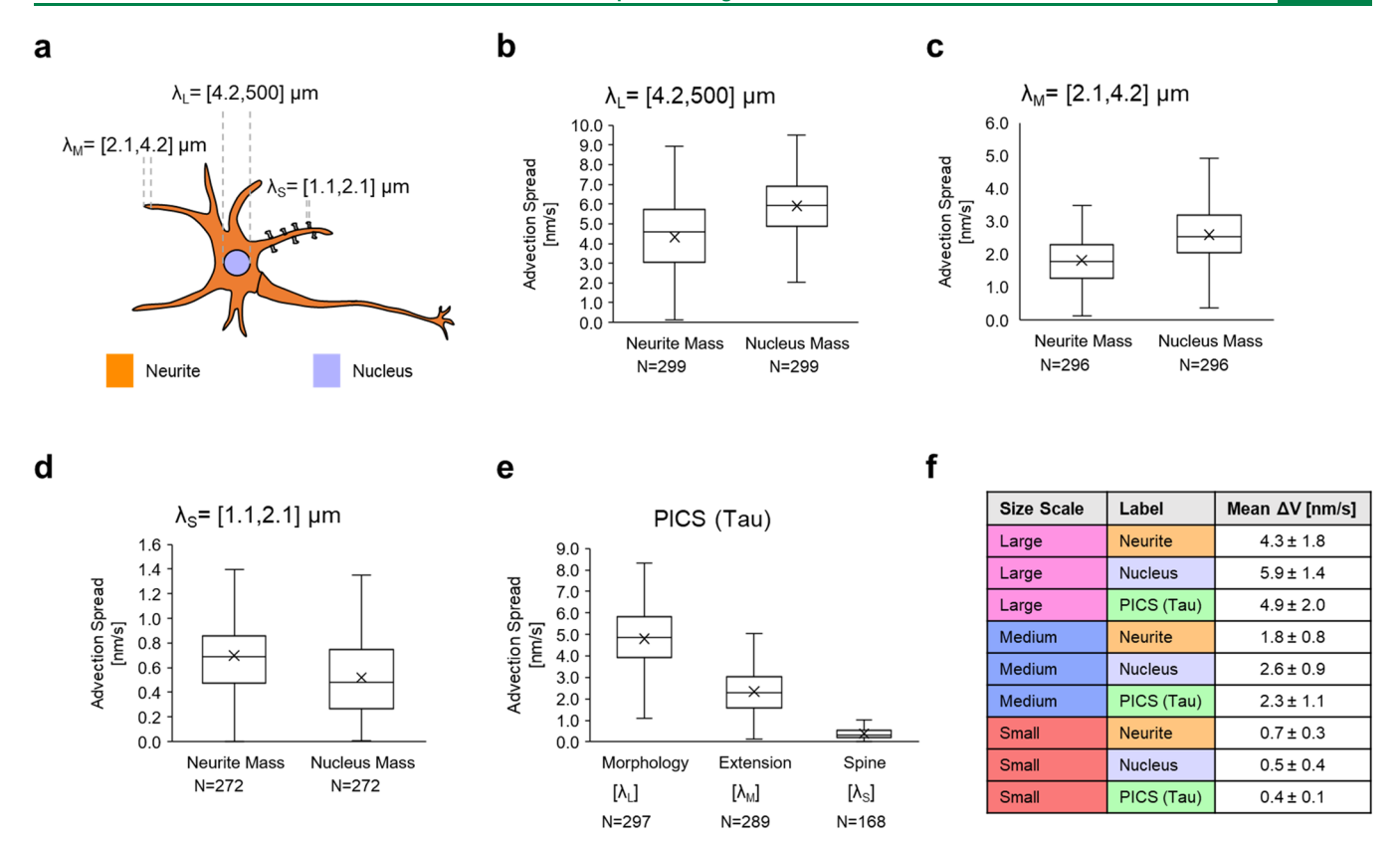


Figure 5. Transport analysis shows substantial nuclear reconfiguration during neuronal arborization. (a) We applied DPS at three spatial scales corresponding to dendritic spines ($\lambda_{Small} = [1.1,2.1] \mu m$), neurites ($\lambda_{Medium} = [2.1,4.2] \mu m$), and cellular morphology ($\lambda_{Large} = [4.2,500] \mu m$). (b-d) By using the semantic segmentation maps generated from PICS, we collected the advection velocity spread corresponding to transport within the neurite and nucleus. Boxplots consist of all fields of view that were found to exhibit active transport, and all differences between categories were statically significant (Mann–Whitney U, *p*-value < 0.05). (e) Transport analysis was run directly on the inferred fluorescence channel. (f) Summary of the dry mass advection spread distributions.

the spatial mode q ($\Gamma \propto q$), and the few sequences that did not meet this model were excluded from our analysis.

Our results for dry-mass transport analysis are summarized in Figure 5f. As a plate read was performed every 48 min, we primarily captured the slow movement consistent with anterograde transport associated with cytoskeletal proteins.⁵⁹ We observed that at a "large" size scale (λ_{I}) associated with cellular morphology, the nucleus-associated mass transport exhibits a 37% higher spread in advective mass transport. Although the spread in mass transport decreases by roughly a factor of 2 in absolute terms, the nucleus-associated mass has a 44% larger spread at scales corresponding to the width of the neuronal extensions ("medium" $\lambda_{\rm M}$). These results hint that despite making up a small fraction of the total mass of the neuronal arbor (roughly 1/4), at scales comparable to cellular morphology and extensions, the nucleus exhibits a remarkable diversity of mass transport activity. This result is in contrast to that for neurites, which are relatively steady in their growth. However, at smaller scales (λ_s) , this relationship becomes reversed with nucleus-associated mass transport showing a 29% smaller spread in velocity coefficients. This is not surprising as smaller scales include neuronal cargo and rapidly moving dendritic spines. All differences were found to be statically significant (Mann–Whitney *U*, *p*-value < 0.05).

Next, we propose to use PICS to measure the transport of the antibody-associated protein rather than the cellular dry mass. The method that extends the transport analysis to fluorescence data is referred to as dispersion-relation

fluorescence spectroscopy.60 However, with PICS, we can study the transport of specific molecular structures without labeling. We selected Tau, as abnormalities in its localization are associated with many cellular pathologies.⁶¹ To calculate these parameters, we substituted the estimated fluorescence signal for the dry mass and computed the DPS advection coefficients associated with the whole field of view. We stress that this type of observation is performed here for the first time, as antibody staining requires destructively fixing the cell. The distribution of transport coefficients is shown in Figure 5e. We note that the DPS transport activity for the Tau protein inferred by PICS is somewhere between the neurite and nucleus activity for size scales corresponding to cellular morphology (λ_L) and extensions (λ_M). Further, the estimated Tau transport is comparably lower for size scales corresponding to dendritic spines (λ_s), which are known to contain less Tau protein when healthy.

Dry Mass Analysis. The PICS approach differentiates itself from the previous efforts on synthetic staining³² by taking a step further and analyzing the cellular dry mass, a measurement that is specific to quantitative phase imaging.¹⁴ We used the Tau/MAP2 semantic segmentation to distinguish the dry mass associated with the nucleus from that of the neurites.

In Figure 6a,b, we measure the normalized rate of change of the dry mass within each of the 300 mosaic tiles (Figure 4a). The results indicate that the neurite mass shows a steady increase, while the growth associated with the nucleus is very low on average, with a high variance in time. To investigate this

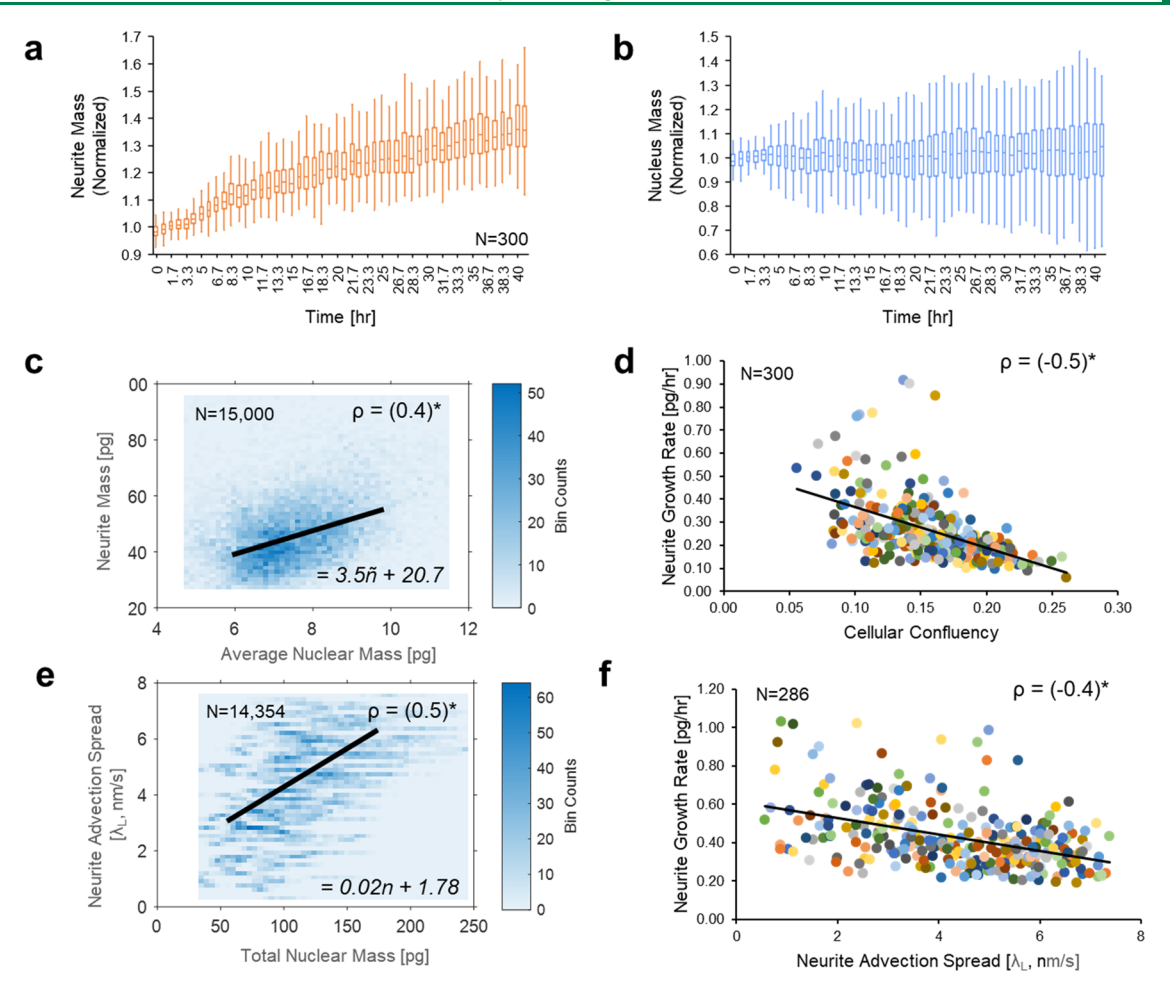


Figure 6. Dry mass analysis for subcellular compartments reveals relationships between growth rates and transport. (a, b) Semantic segmentation maps track the dry mass of nuclei and neurites for 41 h over 300 fields of view, corresponding to approximately 4000 neurons. Dry mass was segregated into nucleus and neurite components by summing the phase values in the GLIM image within the label specified by the PICS map. To extract the relative mass change, these values were normalized by the average dry mass during the first 5 h. While the neurite dry mass shows steady growth, the behavior of the nucleus is more erratic, with no significant growth overall. (c) Neurite mass appears to depend on average nuclear mass ($\rho = 0.4$), with a nuclear count obtained from binary morphological operations at the start of the experiment. (d) Neurite growth rate is negatively related to the cellular confluency ($\rho = -0.5$). Here, we compute the confluency on a per-tile basis by looking at the fraction of the tile occupied by cellular material. (e) Neurite transport behavior for $\lambda_{\rm L}$ depends on the total nuclear mass ($\rho = 0.5$). (f) Neurite growth rate appears to be anti-correlated with advection spread ($\rho = -0.4$).

variability, we looked at the relationship between the average nuclear mass and neurite mass. We calculated the ratio between the per-tile nuclear-associated mass and the nuclear count to obtain the average nucleus mass within the field of view. We noticed an interesting linear relationship between the average nuclear mass and the average neurite mass (Figure 6c), with the average neurite mass being roughly four times the mass of the nucleus ($\rho = 0.4$). Additionally, we observed the expected relationship between neurite growth rates and cellular confluence, which shows that neurites exhibit growth inhibition as their density increases (Figure 6d). For this calculation, the cellular confluence was measured on a per-tile basis at the start of the experiment, and the growth rate was determined by a linear fit.

Finally, we combined the semantic segmentation maps generated by PICS with advection coefficients and growth rates to highlight the interplay between nuclear mass and transport. For each tile, we obtained a coefficient for large-scale transport (λ_L) following the procedure in the previous section. In total, we correlated 15,000 points from all the acquired data. In Figure 6e, we observe a direct relationship between nuclear

mass and transport in neurites ($\rho=0.4$). In contrast, rates of nuclear mass change (growth) were found to be anti-correlated with transport ($\rho=-0.4$). These findings suggest that a more massive nucleus promotes fast traffic in the neurite. At the same time, the transport is slowed down when the neurites grow.

METHODS

Dry Mass Calculation from Phase Images. QPI is governed by a scattering potential that describes how the incident wavefront is distorted by the object. Through a series of pioneering experiments measuring different solutions of proteins and lipids, it was found that dry mass concentration and scattering potential are linearly related. As the scattering potential occurs due to the refractive index difference from the surrounding medium, QPI yields the nonaqueous ("dry") content of the cell.

In conventional microscopes such as DIC or phase contrast, the relationship between the object's scattering potential and the recorded image is not linear. ²⁶ In this case, the recorded image depends on the illumination as well as light propagating from out-of-focus planes. ^{20,26} QPI yields phase maps that are not corrupted by the two amplitudes

of the interfering fields. Thus, the phase image within a given optical section provides access to the dry mass density, σ ,

$$\sigma(\mathbf{r}) = \frac{\lambda}{2\pi\alpha}\phi(\mathbf{r}) \tag{1.1}$$

where λ is the wavelength of light, α is the refractive index increment, and $\phi(\mathbf{r})$ is the quantitative phase image after integration, $\mathbf{r} = (x, y)$.

For correlative analysis, we estimate the rate of dry mass growth by using Savitsky–Golay-based filtering.⁶⁴ Time points lying at the peripheries of the sequence are omitted from analysis.

Neural Network Training. We trained three separate networks to predict Tau, MAP2, and DAPI stains. We used U-Net for the main architecture, as discussed in the "Results" section. The networks for Tau and MAP2 are trained with the colocalized phase and fluorescence image pairs. The outputs of these networks are predicted fluorescence images and are processed into the final semantic segmentation maps, as outlined in the "Methods" section. The model losses for these networks were calculated as the weighted sum of the mean absolute error and the Pearson correlation between the predicted fluorescence intensities and the ground truth fluorescence intensities. Following a standard procedure, pixel values in the image pairs are normalized between 0 and 1, and images are translated by several pixels to account for shifts due to slight misalignments between fluorescent filter cubes. 34

The training, validation, and test split are summarized in Table 1. Initial data were acquired at $20 \times /0.8$ corresponding to $\sim 600 \times 600$

Table 1. Dataset Size

stains	training	validation	test	total	augmentation
Tau/MAP2	784	88	100	972	×4
DAPI	640	80	80	800	×2

 $\mu\mathrm{m}^2$ fields of view. One of the challenges with neural networks is training time, and here we ameliorated these concerns by down-sampling the images by a factor of 2 using nearest neighbor resampling. This procedure is also performed to match the GLIM image to the fluorescence image, which was acquired by 2 \times 2 binning. Next, tiles were divided into quarters. Thus, for estimating the Tau and MAP2 signal, we used 972 phase—fluorescence pairs each corresponding to an area of $\sim\!\!315\times315~\mu\mathrm{m}^2$, with additional augmentation (rotation and flipping) performed on the fly during training.

The network for the DAPI-like nuclear annotation was trained to produce binary labels rather than estimated fluorescence intensities, and the training was performed on a slightly different quantity of images (Table 1). We found that the nuclear annotation required less computation and thus motivated less augmentation and training time.

A commercial workstation running Gentoo⁶⁵ was equipped with two NVIDIA RTX 2070 GPUs, and the networks were implemented using Keras⁶⁶ built on TensorFlow.⁶⁷ We used an ADAM optimizer⁶⁸ with a batch size of one on each GPU, effectively allowing the network to use larger training sizes within a single GPU. Training took 100 epochs and finished in 14 h.

SUMMARY AND DISCUSSION

By combining advanced microscopy with artificial intelligence, PICS allowed us to observe several competing trends during neuronal arborization. We found that for the hippocampal neurons studied in this work, there is a correlation between the average mass of a nucleus and neurites in the same neuron at a preferred dry mass ratio between the two (Figure 6c, roughly a factor of 4). While it was hypothesized that neurons have intrinsic growth potentials in terms of the cellular dry mass, 69 this observation provides direct evidence that, during early network development, the mass within the nucleus balances the mass within the neurite. This hypothesis is further

supported by the interplay of intracellular cellular transport and neurite growth. By limiting our imaging to slow time scales, we focused primarily on anteretrograde transport motion. In Figure 6e, we observe that the dry mass associated with the nuclear mass is directly related to transport activity, with more nuclear mass leading to more active transport in the axons and dendrites. This is not surprising as more massive nuclei are expected to produce more cellular material. Our results highlight that mass transport and growth, two potentially independent phenomena, are anti-correlated in the neurites, where high growth rates appear to be accompanied by slower transport. This observation is in line with the understanding that there exists a metabolic trade-off between cellular motion and vegetative growth.

The complexity of imaging neuronal clusters is primarily due to the photochemical sensitivity of the cells and the resolving power needed to detect fine structures such as dendrites within a developing arbor. To meet these challenges, our approach relies on machine learning, quantitative phase imaging, and transport analysis with few conventional analogs. At the core of our analysis scheme is the use of inferred fluorescence images, which introduce specificity for subcellular compartments through a digital staining procedure (PICS).³⁴ We found that inferring antibody stains requires much more computational complexity compared to simpler markers, such as DAPI. This motivated us to expand the deep-convolutional neuronal network and modify the loss function. Further, we found that the intrinsic variation of protein concentration associated with the MAP2/Tau antibodies made it difficult to generate a semantic segmentation map from the estimated fluorescence signal. This challenge was addressed by using texture-based thresholding to include local image features. Therefore, our approach benefited from splitting the fluorescent estimation and mask generation steps, where the fluorescent estimation could be trained on an unambiguous ground-truth fluorescence image. Further, this approach lets us use the same neural network to impute the signal associated with Tau concentration (Figure 5f).

In a larger context, in contrast to conventional tracking-based approaches for analyzing neuronal extensions (such as Sholl analysis⁷⁴), to improve imaging throughput, we used a continuous model to describe mass transport, which is invariant to annotation errors.

With a plate read performed within a few minutes, PICS enabled us to use label-free microscopes, which are much faster than their fluorescent counterparts. We found that it was roughly 70 times faster to computationally estimate rather than acquire the fluorescence signal. Using the quantitative dry mass output from QPI and the specificity from AI, we were able to compute correlations between neuronal growth rates and intracellular transport, at unprecedented throughput, across thousands of cells.

While in this work we primarily investigated the relationship between nuclei and neurites, we expect that the extension of our mass growth and transport analysis to other stains such as those associated with the specific species of cargo or other cellular systems will be relatively straightforward. Ultimately, by using an interferometric module attached to a conventional DIC microscope and non-confocal epi-fluorescence imaging, we hope that PICS will be broadly adapted as an upgrade to existing microscopes.

ASSOCIATED CONTENT

Supporting Information

The Supporting Information is available free of charge at https://pubs.acs.org/doi/10.1021/acssensors.1c00100.

(Supplementary Note 1) Gradient light interference microscopy; (Supplementary Figure 1) design and calibration of the GLIM module; (Supplementary Note 2) cell culture and immunostaining; (Supplementary Note 3) semantic segmentation accuracy; (Supplementary Table 1) semantic segmentation performance; (Supplementary Figure 2) cellular level detail in GLIM and PICS; (Supplementary Figure 3) semantic segmentation and time-lapse development of the neuronal arbor; (Supplementary Note 4) dispersion-relation phase spectroscopy for mass transport analysis; (Supplementary Figure 4) processing for dispersion-relation phase spectroscopy (PDF)

(Video 1) GLIM and PICS estimated fluorescence for Tau/MAP2/DAPI for the first hippocampal culture; imaging was performed for 41 h at $(20\times/0.8)$ (mp4) (Video 2) GLIM and PICS estimated fluorescence for Tau/MAP2/DAPI for the second hippocampal culture; imaging was performed for 41 h at $(20\times/0.8)$ (mp4) (Video 3) GLIM and PICS estimated fluorescence for Tau/MAP2/DAPI for the third hippocampal culture; imaging was performed for 41 h at $(20\times/0.8)$ (mp4)

AUTHOR INFORMATION

Corresponding Author

Gabriel Popescu — Beckman Institute, University of Illinois at Urbana-Champaign, Urbana, Illinois 61801, United States; Department of Electrical and Computer Engineering, University of Illinois at Urbana-Champaign, Urbana, Illinois 61801, United States; Department of Bioengineering, University of Illinois at Urbana-Champaign, Urbana, Illinois 61801, United States; Phone: (217) 333-4840; Email: gpopescu@illinois.edu

Authors

Mikhail E. Kandel — Beckman Institute, University of Illinois at Urbana-Champaign, Urbana, Illinois 61801, United States; Department of Electrical and Computer Engineering, University of Illinois at Urbana-Champaign, Urbana, Illinois 61801, United States; orcid.org/0000-0003-2124-7750

Eunjae Kim — Beckman Institute, University of Illinois at Urbana-Champaign, Urbana, Illinois 61801, United States; Department of Electrical and Computer Engineering, University of Illinois at Urbana-Champaign, Urbana, Illinois 61801, United States; orcid.org/0000-0003-4854-3197

Young Jae Lee — Beckman Institute and Neuroscience Program, University of Illinois at Urbana-Champaign, Urbana, Illinois 61801, United States; orcid.org/0000-0003-2221-0853

Gregory Tracy – Department of Molecular and Integrative Physiology, University of Illinois at Urbana Champaign, Urbana, Illinois 61801, United States

Hee Jung Chung — Neuroscience Program, University of Illinois at Urbana-Champaign, Urbana, Illinois 61801, United States; Department of Molecular and Integrative Physiology, University of Illinois at Urbana Champaign, Urbana, Illinois 61801, United States

Complete contact information is available at:

https://pubs.acs.org/10.1021/acssensors.1c00100

Author Contributions

*M.E.K. and E.K. contributed equally to this work. M.E.K. designed and performed imaging experiments. G.T. dissected cortices from rat E18 embryos. Y.J.L. cultured and stained hippocampal neurons. H.J.C. contributed reagents and animals. E.K. developed and trained the neural network. M.E.K. and E.K. performed analysis. M.E.K., E.K., and G.P. wrote the manuscript. G.P. supervised the project.

Notes

The authors declare the following competing financial interest(s): G.P. has a financial interest in Phi Optics, Inc., a company developing GLIM and PICS for materials and life science applications. The remaining authors declare no competing interests.

The data that support the findings of this study are available upon reasonable request.

The code and computer algorithms that support the findings of this study are available from the corresponding author upon reasonable request.

ACKNOWLEDGMENTS

This work is supported by NSF 0939511 (G.P.), R01GM129709 (G.P.), R01 CA238191 (G.P.), R43GM133280-01 (G.P.), R01NS083402 (H.J.C), and R01NS097610 (H.J.C). M.E.K. is supported by a fellowship from the Miniature Brain Machinery Program at UIUC (NSF, NRT-UtB, and 1735252).

REFERENCES

- (1) Kweon, J. H.; Kim, S.; Lee, S. B. The cellular basis of dendrite pathology in neurodegenerative diseases. *BMB Rep.* **2017**, *50*, 5–11.
- (2) Prior, M.; Chiruta, C.; Currais, A.; Goldberg, J.; Ramsey, J.; Dargusch, R.; Maher, P. A.; Schubert, D. Back to the future with phenotypic screening. *ACS Chem. Neurosci.* **2014**, *5*, 503–513.
- (3) Pruss, R. M. Phenotypic screening strategies for neuro-degenerative diseases: a pathway to discover novel drug candidates and potential disease targets or mechanisms. CNS Neurol. Disord.: Drug Targets 2010, 9, 693–700.
- (4) Götte, M.; Hofmann, G.; Michou-Gallani, A.-I.; Glickman, J. F.; Wishart, W.; Gabriel, D. An imaging assay to analyze primary neurons for cellular neurotoxicity. *J. Neurosci. Methods* **2010**, *192*, 7–16.
- (5) Garay, P. M.; Holtz, N.; Groppi, V.; McGillicuddy, L. CellPlayerTM 96-Well Kinetic NeuroTrackTM Assay.
- (6) Brown, J.; Garay, T.; Alcantara, S. L.; McGillicuddy, L.; Holtz, N.; Rauch, J.; McEwen, D.; Groppi, V.; Dale, T.; McManus, O. Measuring Neurite Dynamics in Co-culture Using IncuCyte ZOOM® Live-content Imaging Platform and NeuroLight RedTM Fluorescent Label; 2015
- (7) Wilt, B. A.; Burns, L. D.; Wei Ho, E. T.; Ghosh, K. K.; Mukamel, E. A.; Schnitzer, M. J. Advances in light microscopy for neuroscience. *Annu. Rev. Neurosci.* **2009**, *32*, 435–506.
- (8) Kim, B. G.; Dai, H.-N.; McAtee, M.; Vicini, S.; Bregman, B. S. Labeling of dendritic spines with the carbocyanine dye Dil for confocal microscopic imaging in lightly fixed cortical slices. *J Neurosci Methods* **2007**, *162*, 237–243.
- (9) Shlevkov, E.; Basu, H.; Bray, M.-A.; Sun, Z.; Wei, W.; Apaydin, K.; Karhohs, K.; Chen, P.-F.; Smith, J. L. M.; Wiskow, O.; Roet, K.; Huang, X.; Eggan, K.; Carpenter, A. E.; Kleiman, R. J.; Schwarz, T. L. A High-Content Screen Identifies TPP1 and Aurora B as Regulators of Axonal Mitochondrial Transport. *Cell Rep.* **2019**, 28, 3224—3237.e5.
- (10) Icha, J.; Weber, M.; Waters, J. C.; Norden, C. Phototoxicity in live fluorescence microscopy, and how to avoid it. *BioEssays* **2017**, *39*, 1700003.

- (11) Sanderson, M. J.; Smith, I.; Parker, I.; Bootman, M. D. Fluorescence microscopy. Cold Spring Harbor Protocols. *Cold Spring Harbor Protoc.* **2014**, *2015*, 1042–1065.
- (12) Karra, D.; Dahm, R. Transfection techniques for neuronal cells. *J. Neurosci.* **2010**, *30*, 6171–6177.
- (13) Popescu, G. Quantitative phase imaging of cells and tissues; McGraw Hill Professional: 2011.
- (14) Park, Y.; Depeursinge, C.; Popescu, G. Quantitative phase imaging in biomedicine. *Nat. Photonics* **2018**, *12*, 578–589.
- (15) Chen, X.; Kandel, M. E.; Popescu, G. Spatial light interference microscopy (SLIM): principle and applications to biomedicine. *arXiv* preprint arXiv:2012.08801 **2020**.
- (16) Mir, M.; Wang, Z.; Shen, Z.; Bednarz, M.; Bashir, R.; Golding, I.; Prasanth, S. G.; Popescu, G. Optical measurement of cycle-dependent cell growth. *Proc. Natl. Acad. Sci.* **2011**, *108*, 13124–13129
- (17) Tian, L.; Liu, Z.; Yeh, L.-H.; Chen, M.; Zhong, J.; Waller, L. Computational illumination for high-speed *in vitro* Fourier ptychographic microscopy. *Optica* **2015**, *2*, 904–911.
- (18) Kim, D.; Lee, S.; Lee, M.; Oh, J.; Yang, S.-A.; Park, Y. Refractive index as an intrinsic imaging contrast for 3-D label-free live cell imaging. *BioRxiv* **2017**, 106328.
- (19) Kastl, L.; Isbach, M.; Dirksen, D.; Schnekenburger, J.; Kemper, B. Quantitative phase imaging for cell culture quality control. *Cytometry, Part A* **2017**, *91*, 470–481.
- (20) Kandel, M. E.; Teng, K. W.; Selvin, P. R.; Popescu, G. Labelfree imaging of single microtubule dynamics using spatial light interference microscopy. *ACS Nano* **2017**, *11*, 647–655.
- (21) Kim, K.; Yoon, J.; Shin, S.; Lee, S.; Yang, S.-A.; Park, Y. Optical diffraction tomography techniques for the study of cell pathophysiology. *J. Biomed. Photonics Eng.* **2016**, *2*, No. 020201.
- (22) Chen, X.; Kandel, M. E.; Hu, C.; Lee, Y. J.; Popescu, G. Wolf phase tomography (WPT) of transparent structures using partially coherent illumination. *Light: Sci. Appl.* **2020**, *9*, 142.
- (23) Dardikman-Yoffe, G.; Mirsky, S. K.; Barnea, I.; Shaked, N. T. High-resolution 4-D acquisition of freely swimming human sperm cells without staining. *Sci. Adv.* **2020**, *6*, eaay7619.
- (24) Kandel, M. E.; Sridharan, S.; Liang, J.; Luo, Z.; Han, K.; Macias, V.; Shah, A.; Patel, R.; Tangella, K.; Kajdacsy-Balla, A.; Guzman, G.; Popescu, G. Label-free tissue scanner for colorectal cancer screening. *J. Biomed. Opt.* **2017**, 22, No. 066016.
- (25) Chen, M.; Tian, L.; Waller, L. 3D differential phase contrast microscopy. *Biomed. Opt. Express* **2016**, *7*, 3940–3950.
- (26) Nguyen, T. H.; Kandel, M. E.; Rubessa, M.; Wheeler, M. B.; Popescu, G. Gradient light interference microscopy for 3D imaging of unlabeled specimens. *Nat. Commun.* **2017**, *8*, 210.
- (27) Rubessa, M.; Feugang, J. M.; Kandel, M. E.; Schreiber, S.; Hessee, J.; Salerno, F.; Meyers, S.; Chu, I.; Popescu, G.; Wheeler, M. B. High-throughput sperm assay using label-free microscopy: morphometric comparison between different sperm structures of boar and stallion spermatozoa. *Anim. Reprod. Sci.* **2020**, 219, 106509.
- (28) Nygate, Y. N.; Levi, M.; Mirsky, S. K.; Turko, N. A.; Rubin, M.; Barnea, I.; Dardikman-Yoffe, G.; Shalev, A.; Shaked, N. T. HoloStain: Holographic virtual staining of individual biological cells. *arXiv* preprint arXiv:1909.11374 **2019**.
- (29) Dubey, V.; Popova, D.; Ahmad, A.; Acharya, G.; Basnet, P.; Mehta, D. S.; Ahluwalia, B. S. Partially spatially coherent digital holographic microscopy and machine learning for quantitative analysis of human spermatozoa under oxidative stress condition. *Sci. Rep.* **2019**, *9*, 3564.
- (30) Rawat, W.; Wang, Z. Deep Convolutional Neural Networks for Image Classification: A Comprehensive Review. *Neural Comput.* **2017**, 29, 2352–2449.
- (31) Isola, P.; Zhu, J.-Y.; Zhou, T.; Efros, A. A. Image-to-image translation with conditional adversarial networks. In *Proceedings of the IEEE conference on computer vision and pattern recognition*; 2017; pp. 1125–1134.
- (32) Christiansen, E. M.; Yang, S. J.; Ando, D. M.; Javaherian, A.; Skibinski, G.; Lipnick, S.; Mount, E.; O'Neil, A.; Shah, K.; Lee, A. K.;

- Goyal, P.; Fedus, W.; Poplin, R.; Esteva, A.; Berndl, M.; Rubin, L. L.; Nelson, P.; Finkbeiner, S. *In Silico* Labeling: Predicting Fluorescent Labels in Unlabeled Images. *Cell* **2018**, *173*, 792–803.e19.
- (33) Rivenson, Y.; Wang, H.; Wei, Z.; de Haan, K.; Zhang, Y.; Wu, Y.; Günaydın, H.; Zuckerman, J. E.; Chong, T.; Sisk, A. E.; Westbrook, L. M.; Wallace, W. D.; Ozcan, A. Virtual histological staining of unlabelled tissue-autofluorescence images via deep learning. *Nat. Biomed. Eng.* **2019**, *3*, 466–477.
- (34) Kandel, M. E.; He, Y. R.; Lee, Y. J.; Chen, T. H.-Y.; Sullivan, K. M.; Aydin, O.; Saif, M. T. A.; Kong, H.; Sobh, N.; Popescu, G. Phase imaging with computational specificity (PICS) for measuring dry mass changes in sub-cellular compartments. *Nat. Commun.* **2020**, *11*, 6256.
- (35) Kandel, M. E.; Rubessa, M.; He, Y. R.; Schreiber, S.; Meyers, S.; Matter Naves, L.; Sermersheim, M. K.; Sell, G. S.; Szewczyk, M. J.; Sobh, N.; Wheeler, M. B.; Popescu, G. Reproductive outcomes predicted by phase imaging with computational specificity of spermatozoon ultrastructure. *Proc. Natl. Acad. Sci.* **2020**, *117*, 18302—18309.
- (36) Chung, H.; Huh, J.; Kim, G.; Park, Y. K.; Ye, J. C. Unsupervised Missing Cone Deep Learning in Optical Diffraction Tomography. arXiv preprint arXiv:2103.09022 2021.
- (37) Liu, T.; de Haan, K.; Bai, B.; Rivenson, Y.; Luo, Y.; Wang, H.; Karalli, D.; Fu, H.; Zhang, Y.; FitzGerald, J.; Ozcan, A. Deep learning-based holographic polarization microscopy. *ACS Photonics* **2020**, *7*, 3023–3034.
- (38) Pinkard, H.; Phillips, Z.; Babakhani, A.; Fletcher, D. A.; Waller, L. Deep learning for single-shot autofocus microscopy. *Optica* **2019**, *6*, 794–797.
- (39) Choi, G.; Ryu, D.; Jo, Y.; Kim, Y. S.; Park, W.; Min, H.-s.; Park, Y. Cycle-consistent deep learning approach to coherent noise reduction in optical diffraction tomography. *Opt. Express* **2019**, *27*, 4927–4943.
- (40) Jiao, Y.; He, Y. R.; Kandel, M. E.; Liu, X.; Lu, W.; Popescu, G. Computational interference microscopy enabled by deep learning. arXiv preprint arXiv:2012.10239 2020.
- (41) Kosik, K. S.; Finch, E. A. MAP2 and tau segregate into dendritic and axonal domains after the elaboration of morphologically distinct neurites: an immunocytochemical study of cultured rat cerebrum. *J. Neurosci.* **1987**, *7*, 3142–3153.
- (42) Sullivan, K. M.; Park, C. G.; Ito, J. D.; Kandel, M.; Popescu, G.; Kim, Y. J.; Kong, H. Matrix Softness-Mediated 3D Zebrafish Hepatocyte Modulates Response to Endocrine Disrupting Chemicals. *Environ. Sci. Technol.* **2020**, *54*, 13797–13806.
- (43) Kandel, M. E.; Hu, C.; Kouzehgarani, G. N.; Min, E.; Sullivan, K. M.; Kong, H.; Li, J. M.; Robson, D. N.; Gillette, M. U.; Best-Popescu, C.; Popescu, G. Epi-illumination gradient light interference microscopy for imaging opaque structures. *Nat. Commun.* **2019**, *10*, 4691.
- (44) Dehmelt, L.; Halpain, S. The MAP2/Tau family of microtubule-associated proteins. *Genome Biol.* **2005**, *6*, 204.
- (45) Movellan, J. R. Tutorial on Gabor filters. Open Source Document 2002.
- (46) Wold, S.; Esbensen, K.; Geladi, P. Principal component analysis. *Chemom. Intell. Lab. Syst.* **1987**, *2*, 37–52.
- (47) Št, O.; Beneš, B. Connected component labeling in CUDA. In GPU computing gems emerald edition; Elsevier: 2011; pp. 569–581.
- (48) Ronneberger, O.; Fischer, P.; Brox, T. U-net: Convolutional networks for biomedical image segmentation. In *CInternational onference on Medical image computing and computer-assisted intervention*; Springer: 2015; pp. 234–241.
- (49) Weisstein, E. W. L^ 1-Norm; 2000.
- (50) Ledig, C.; Theis, L.; Huszár, F.; Caballero, J.; Cunningham, A.; Acosta, A.; Aitken, A.; Tejani, A.; Totz, J.; Wang, Z. Photo-realistic single image super-resolution using a generative adversarial network. In *Proceedings of the IEEE conference on computer vision and pattern recognition*; 2017; pp. 4681–4690.

- (51) Antun, V.; Renna, F.; Poon, C.; Adcock, B.; Hansen, A. C. On instabilities of deep learning in image reconstruction-Does AI come at a cost? *arXiv preprint arXiv:1902.05300* **2019**.
- (52) Benesty, J.; Chen, J.; Huang, Y.; Cohen, I. Pearson correlation coefficient. In *Noise reduction in speech processing*; Springer: 2009; pp. 1–4.
- (53) Stice, S. L. Human embryonic stem cells provide a robust source of neural cells for drug discovery and toxicity. *J. Pharmacol. Toxicol. Methods* **2009**, *2*, 259.
- (54) Al-Ali, H.; Blackmore, M.; Bixby, J. L.; Lemmon, V. P., High Content Screening with Primary Neurons. In *Assay Guidance Manual*; Markossian, S., Sittampalam, G. S., Grossman, A., Brimacombe, K.; Arkin, M.; Auld, D., Austin, C. P., Baell, J., Caaveiro, J. M. M., Chung, T. D. Y., Coussens, N. P., Dahlin, J. L., Devanaryan, V., Foley, T. L., Glicksman, M., Hall, M. D., Haas, J. V., Hoare, S. R. J., Inglese, J., Iversen, P. W., Kahl, S. D., Kales, S. C., Kirshner, S., Lal-Nag, M., Li, Z., McGee, J., McManus, O., Riss, T., Saradjian, P., Trask, O. J., Jr., Weidner, J. R., Wildey, M. J., Xia, M., Xu, X. Eds.; Eli Lilly & Company and the National Center for Advancing Translational Sciences: Bethesda (MD), 2004.
- (55) Khoshakhlagh, P.; Bowser, D. A.; Brown, J. Q.; Moore, M. J. Comparison of visible and UVA phototoxicity in neural culture systems micropatterned with digital projection photolithography. *J. Biomed. Mater. Res., Part A* **2019**, *107*, 134–144.
- (56) Wessells, N. K.; Letourneau, P. C.; Nuttall, R. P.; Ludueña-Anderson, M.; Geiduschek, J. M. Responses to cell contacts between growth cones, neurites and ganglionic non-neuronal cells. *J Neurocytol.* **1980**, *9*, 647–664.
- (57) Wang, R.; Wang, Z.; Millet, L.; Gillette, M. U.; Levine, A. J.; Popescu, G. Dispersion-relation phase spectroscopy of intracellular transport. *Opt. Express* **2011**, *19*, 20571–20579.
- (58) Cintora, P.; Arikkath, J.; Kandel, M.; Popescu, G.; Best-Popescu, C. Cell density modulates intracellular mass transport in neural networks. *Cytometry, Part A* **2017**, *91*, 503–509.
- (59) Maday, S.; Twelvetrees, A. E.; Moughamian, A. J.; Holzbaur, E. L. F. Axonal transport: cargo-specific mechanisms of motility and regulation. *Neuron* **2014**, *84*, 292–309.
- (60) Wang, R.; Lei, L.; Wang, Y.; Levine, A. J.; Popescu, G. Dispersion-relation fluorescence spectroscopy. *Phys. Rev. Lett.* **2012**, 109, 188104.
- (61) Mandelkow, E. M.; Stamer, K.; Vogel, R.; Thies, E.; Mandelkow, E. Clogging of axons by tau, inhibition of axonal traffic and starvation of synapses. *Neurobiol. Aging* **2003**, *24*, 1079–1085.
- (62) Hoover, B. R.; Reed, M. N.; Su, J.; Penrod, R. D.; Kotilinek, L. A.; Grant, M. K.; Pitstick, R.; Carlson, G. A.; Lanier, L. M.; Yuan, L.-L.; Ashe, K. H.; Liao, D. Tau mislocalization to dendritic spines mediates synaptic dysfunction independently of neurodegeneration. *Neuron* 2010, 68, 1067–1081.
- (63) Barer, R. Interference microscopy and mass determination. *Nature* **1952**, *169*, 366–367.
- (64) Ramos, T. Savitsky-Golay based filtering and first derivative. https://www.mathworks.com/matlabcentral/fileexchange/51938-savitsky-golay-based-filtering-and-first-derivative.
- (65) Ioanas, H.-I.; Saab, B.; Rudin, M. Gentoo Linux for Neuroscience-a replicable, flexible, scalable, rolling-release environment that provides direct access to development software. *Res. Ideas Outcomes* **2017**, *3*, e12095.
- (66) Chollet, F. keras. 2015.
- (67) Abadi, M.; Barham, P.; Chen, J.; Chen, Z.; Davis, A.; Dean, J.; Devin, M.; Ghemawat, S.; Irving, G.; Isard, M. Tensorflow: A system for large-scale machine learning In 12th {USENIX} Symposium on Operating Systems Design and Implementation ({OSDI} 16); 2016; pp. 265–283.
- (68) Kingma, D. P.; Ba, J. Adam: A method for stochastic optimization. arXiv preprint arXiv:1412.6980 2014.
- (69) Corbin, E. A.; Millet, L. J.; Keller, K. R.; King, W. P.; Bashir, R. Measuring physical properties of neuronal and glial cells with resonant microsensors. *Anal. Chem.* **2014**, *86*, 4864–4872.

- (70) Fanous, M. J.; Li, Y.; Kandel, M. E.; Abdeen, A. A.; Kilian, K. A.; Popescu, G. Effects of substrate patterning on cellular spheroid growth and dynamics measured by gradient light interference microscopy (GLIM). *J. Biophotonics* **2019**, *12*, e201900178.
- (71) Vasdekis, A. E.; Alanazi, H.; Silverman, A. M.; Williams, C. J.; Canul, A. J.; Cliff, J. B.; Dohnalkova, A. C.; Stephanopoulos, G. Eliciting the impacts of cellular noise on metabolic trade-offs by quantitative mass imaging. *Nat. Commun.* **2019**, *10*, 848.
- (72) Bertels, J.; Rubessa, M.; Kandel, M. E.; Bane, T.; Milner, D. J.; Popescu, G.; Wheeler, M. B. Zinc's Effect on the Differentiation of Porcine Adipose-derived Stem Cells into Osteoblasts. *J. Regener. Med.* **2019**, *8*, 2.
- (73) Kim, J.; Darlington, A.; Salvador, M.; Utrilla, J.; Jiménez, J. I. Trade-offs between gene expression, growth and phenotypic diversity in microbial populations. *Curr. Opin. Biotechnol.* **2020**, *62*, 29–37.
- (74) Sholl, D. A. Dendritic organization in the neurons of the visual and motor cortices of the cat. *J. Anat.* 1953, 87, 387–406.